

# The effects of nose-shape and upstream flow separation on the wake of a cylindrical square-backed body

Gershom Easanesan\*, David Burton, Mark C. Thompson

*Department of Mechanical and Aerospace Engineering, Monash University, Clayton, Australia*

---

## Abstract

An experimental study was conducted on flow around two-dimensional, square-backed bluff bodies in the presence of a ground plane. Two frontal geometries were tested: one with significant leading-edge separation and one without. The extensive leading-edge separation was found to induce significant asymmetry in the time-averaged wake. One-sided shedding from the top trailing edge was found to occur in the absence of significant separation, but broad-spectrum turbulence was found to be responsible for much of the fluctuating energy. More pronounced upstream separation was found to further inhibit regular shedding of large-scale structures in the wake. Over the range considered, a degree of Reynolds number sensitivity was observed, with the boundary layer along the ground plane separating upstream of the body at low Reynolds numbers. The effect of increasing the ground clearance was also considered, which weakened the leading-edge separation whilst increasing the prominence of vortex shedding.

*Keywords:* Bluff body, Flow separation, PIV, Square-back, Ground proximity

---

## 1. Introduction

Due to the commercial requirement of maximising cargo capacity, square-backed geometries are common among heavy transport vehicles. These geometries tend to produce pronounced regions of separation in the wake, which contribute significantly to the drag. The potential gains for drag reduction has generated considerable interest in this area, with work often focused on simplified square-backed models with the aim of reaching more widely applicable conclusions.

Among the most prevalent of such geometries is the Ahmed body, popularised by Ahmed et al. [3]. The slant angle on the rear of the body has a marked effect on the composition of the wake, with the zero-degree slant-angle case, which is of interest in this study, no longer possessing a wake dominated by the pair of counter-rotating vortices emanating from the sides of the body seen at higher slant angles. Instead, Grandemange et al. [11], in providing a thorough characterization of the wake of this geometry, notes the presence of a large region of separation composed of a complex mix of coherent and incoherent structures, including weak vortex shedding due to the interaction between the vertical and lateral shear layers. Further adding to the complexity of the flow is the bi-stability of the wake over long time-scales, which results in one-sided shedding in the lateral direction [11].

Given the complexity of the wake flow topology, it would seem beneficial to isolate the effects of individual shear-layer interactions, as improved understanding of these effects would prove advantageous in designing better targeted flow control techniques. A reasonable body of work does exist on symmetric 2D square-backed bodies (16, 17, 12, 5, 14 and 15). However, of these only Parkin et al. [15] considers the influence of the ground plane on the wake.

Prominently, away from the ground plane, the wake dynamics include coherent vortex shedding that is virtually absent for a body in proximity to the ground. The characteristics of this feature has long been linked to the base pressure and as a result, the drag of bluff bodies (5). It is therefore of interest to observe the change in these aspects of the wake as the upstream conditions of the flow are altered. In this respect, the studies conducted on bodies away from the ground have displayed a degree of insensitivity to the nose shape. In particular, Bearman [5] and Park et al. [14] looked at elliptical-nosed bodies with axis ratios of 10:1 and 8:1 respectively, at Reynolds numbers of approximately  $4 \times 10^4$ , while Pastoor et al. [17] studied a D-shaped at a range of Reynolds numbers including  $3.5 \times 10^4$  and  $4.6 \times 10^4$ . Prominent vortex shedding was observed across all nose geometries, with the Strouhal number ranging between 0.23 and 0.25. Variation in the base pressure was also small, ranging from -0.52 to -0.57. Of note here is the relative similarity of the boundary layer momentum thickness approaching the trailing edge, which varied from 0.014 to 0.017. In contrast to the away-from-ground case, it is yet unclear how the nose shape affects the wake properties of these geometries in proximity to

---

\*Corresponding author

Email address: samuel.easanesan@monash.edu (Gershom Easanesan)

60  
61  
62  
63 the ground, particularly in the context of reduced coherent  
64 vortex shedding.

65 In addition to the reduction of coherent shedding, Parkin  
66 et al. [15] highlighted a number of other changes imposed  
67 on the flow by the ground plane. Unsurprisingly, the hor-  
68 izontal centreplane symmetry of the flow is broken, begin-  
69 ning with the stagnation point moving lower, continuing  
70 with the above body recirculation region growing in size,  
71 whilst the corresponding recirculation region below the  
72 body ceases to exist, and culminating in a highly asym-  
73 metric wake, due to the disparity between the roll-up of  
74 the two shear layers.

75 It should be noted that not all these features remain  
76 present for the three-dimensional Ahmed body. Promi-  
77 nently, results from Grandemange et al. [11] suggest the  
78 time-averaged wake in the symmetry plane retains a no-  
79 ticeably more symmetric structure. Furthermore, while  
80 the stagnation point does remain below the centreline, the  
81 flow does continue to separate from the lower surface of  
82 the body, albeit with a shorter recirculation length. The  
83 extent of flow separation over the nose does appear to vary  
84 across studies, with Bonnavion [8] reporting an absence of  
85 flow separation at the nose of the body at experiments con-  
86 ducted at  $Re \approx 4 \times 10^5$ , warranting further examination  
87 of its effects on the wake.

88 The scarcity of prior research on two-dimensional square-  
89 backed bodies in proximity to the ground also includes the  
90 lack of consideration of Reynolds number effects. Nev-  
91 ertheless, some clues to the possible wake response may  
92 be found from more commonly studied analogous geome-  
93 tries. For instance, in wind-tunnel experiments on the  
94 flow over a backward-facing step, Adams and Johnston [2]  
95 studied the effect of both boundary layer thickness and  
96 Reynolds number, with the latter ranging from  $8 \times 10^3$  to  
97  $4 \times 10^4$ . The reattachment length was found to vary with  
98 Reynolds number throughout the range tested, peaking  
99 at a Reynolds number of  $2 \times 10^4$  for a turbulent separ-  
100 ating boundary layer. A weak trend of the reattachment  
101 length decreasing with boundary layer thickness growth  
102 was also observed for the turbulent boundary layer case.  
103 Varying levels of Reynolds number insensitivity have pre-  
104 viously been reported for related geometries. For instance,  
105 in the case of the two-dimensional Ahmed body away from  
106 the ground, Pastoor et al. [17] found that base pressure  
107 and Strouhal number remained stable for Reynolds num-  
108 bers between  $2.3 \times 10^4$  and  $7 \times 10^4$ , whilst in relation  
109 to three-dimensional bluff bodies, Spohn and Gilliron [20]  
110 reported good agreement between experiments conducted  
111 at Reynolds numbers of  $O(10^3)$  and studies conducted at  
112  $O(10^6)$  in the context of wake flow topology behind a  $25^\circ$   
113 slant angle Ahmed body. This is despite Grandemange  
114 et al. [11] identifying a decline in the size of the front sepa-  
115 ration bubble as the Reynolds number was increased. This  
116 latter observation would indicate that some useful insights  
117 into the flow around the two-dimensional Ahmed body in  
118 the presence of a ground surface may be gleaned from vary-  
ing the Reynolds number, given the increased region of

separated flow above the body as discussed beforehand.

With regards to the transient characteristics of the  
flow, Parkin et al. [15] demonstrated the ground plane's  
role in reducing periodicity in the wake. This breakup of  
organized wake structures has also been profiled for other  
geometries such as circular cylinders [18]. It should be  
noted here that extensive overbody separation has also  
been known to affect the dynamics of the wake. Taylor  
et al. [21] for instance, when considering cylinders with  
variable leading and trailing edges, found that vortex shed-  
ding was noticeably weaker and more intermittent for cylin-  
ders with rectangular ends in comparison to circular and  
triangular ends, which produced less pronounced separa-  
tion over the sides of the cylinder. The effects of recir-  
culation bubbles upstream of fixed separation points can  
also be observed in the results of Minelli et al. [13], who  
looked at actuation around the A-pillars of a truck, discov-  
ering that the time-averaged wake lengthened appreciably  
as the bubble grew. Given the prominence of the recircula-  
tion bubble above the body described by Parkin et al. [15],  
it is of interest to understand the extent to which this al-  
ters the formation of coherent structures in the wake. The  
present study seeks to resolve this question, in addition  
to documenting the wider effects of the above-body recir-  
culation on the flow topology of the wake. In short, this  
study focuses on two main points: how leading-edge sep-  
aration induced by nose geometry affects the wake flow of  
cylindrical bodies; and how these effects are influenced by  
ground proximity and Reynolds number.

## 2. Methodology

The experiments were conducted in the Monash Uni-  
versity Fluids Laboratory for Aeronautical and Industrial  
Research (FLAIR) water channel, located on the univer-  
sity campus in Clayton, Australia. The water channel is  
4000 mm long and has a cross-sectional width and height  
of 600 mm and 800 mm, respectively.

The model used consisted of a square-backed geome-  
try with an interchangeable nose configuration and was  
constructed from acrylic. The model extended 400 mm in  
the spanwise direction and had a height,  $H$ , of 50 mm,  
yielding an aspect ratio (span to height) of 8. Of the two  
configurations tested, the first resembled an Ahmed body  
cross-section with a 0 degree back-slant angle, and had a  
length of  $3.64H$  from the leading edge to the trailing edge.  
The second configuration used an elliptical nose with a  
3:1 length-height ratio. In this configuration, the model  
measured  $4.8H$  between the leading and trailing edges.

The model was mounted in proximity to a ground plane  
initially located  $0.2H$  above from model as depicted in  
Figure 1. This ground clearance is the identical to that  
used by Parkin et al. [15] and slightly higher than the  
 $0.17H$  utilised by Grandemange et al. [11]. In addition  
to this, ground clearances of  $0H$ ,  $0.4H$  and  $4.2H$  were  
also tested in limited quantities, with the last of these  
approximating the away-from-ground case. The leading

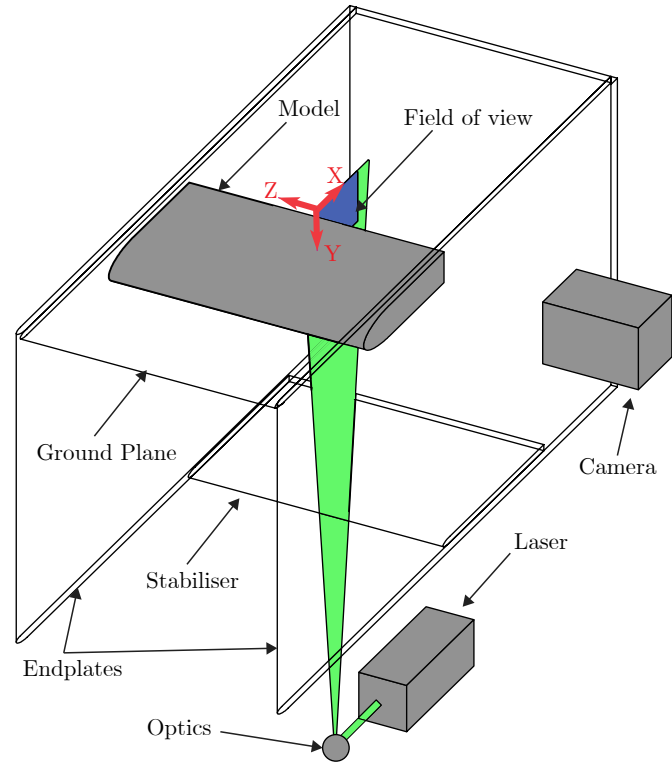


Figure 1: Diagram of the layout of the experimental setup for capturing snapshots of the wake behind the elliptical-nosed body. The  $X$ -directional positions of the laser and camera were varied for other fields of view.

edge of the ground plane was elliptical with a 4:1 axis ratio and was located  $6.74H$  upstream of the nose of the model for both nose configurations. The model and the ground plane were mounted to endplates on each side. These were mounted flush against the model and the ground plane, and extended  $10H$  in the vertical direction. An additional stabiliser panel was added at the foot of the endplates to suppress oscillations of the endplates. Tests were primarily conducted at a channel velocity of  $0.4 \text{ ms}^{-1}$ , yielding a Reynolds number,  $Re$ , based on model height, of  $2 \times 10^4$ . Additional tests were also conducted at Reynolds numbers of  $1 \times 10^4$  and  $5 \times 10^3$ .

Throughout this paper,  $X$  is taken as the longitudinal direction and  $Y$  as the vertical direction. The origin is taken at the surface of the ground plane at the location of the base of the model unless specified otherwise.

Particle-image velocimetry (PIV) was undertaken on the models, the methodology of which has been extensively covered elsewhere (e.g. see 19). Spherical glass particles (Vestosint) with a mean size of  $56 \mu\text{m}$  and density of  $1.016 \text{ kgm}^{-3}$  were used to seed the flow. The particles were illuminated by a 5 W continuous argon-ion laser, with the beam spread into a 2 mm thick laser sheet. Images were captured using a PCO Dimax.S4 CMOS camera with a resolution of  $2016 \times 2016$ , utilising both a 105 mm and 50 mm lens. In-house cross-correlation software was used to analyse the images, adapted from the techniques

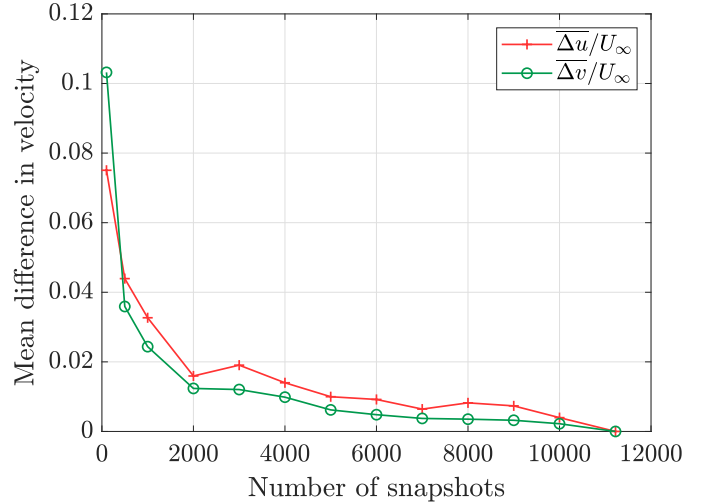


Figure 2: Convergence of mean difference in time-averaged velocity for increasing number of image pairs relative to values using all image pairs.

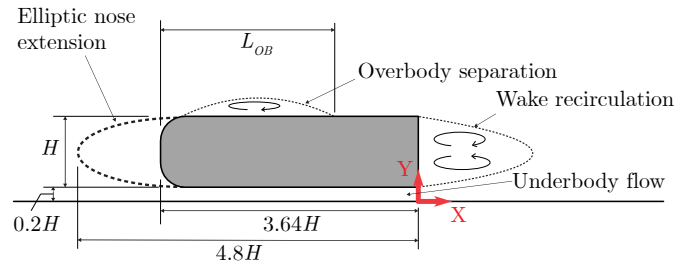


Figure 3: Diagram highlighting key dimensions and flow features for the Ahmed-body cross-section for the  $0.2H$  ground clearance case.

described by Fouras et al. [10]. A  $32 \times 32$  pixel window size, with an overlap of 50% was used to determine the velocity components. For the time-averaged statistics, the spatial resolution of the velocity fields was  $0.03H$ . In order to capture the formation and advection of large-scale structures in the wake, a wider image size was required when conducting proper orthogonal decomposition (POD) on the velocity fields. This necessitated a decrease in the spatial resolution of these analyses to  $0.09H$ , which remained sufficient to capture the large-scale structures of interest.

Time-averaged spanwise ( $XZ$  plane) measurements of the top shear layer were undertaken to assess the spanwise variation across the model. Variation in the streamwise velocity across the central  $4H$  of the model was limited to  $0.02U_\infty$ , with spanwise velocities recorded in the range of  $\pm 0.006U_\infty$ . A minimum of 9171 image pairs were utilised when constructing the time-averaged velocity fields for all cases, with over 10000 pairs utilised in most instances. Convergence was assessed by monitoring the mean change in the time-averaged velocity components relative to the values computed over all image pairs over an increasing number of snapshots. Convergence to within  $0.03U_\infty$  was generally observed within 2000 image pairs (Figure 2).

Contributions to the overall uncertainty from sources

178  
179  
180  
181  
182  
183  
184  
185  
186  
187  
188  
189  
190  
191  
192  
193  
194  
195  
196  
197  
198  
199  
200  
201  
202  
203  
204  
205  
206  
207  
208  
209  
210  
211  
212  
213  
214  
215  
216  
217  
218  
219  
220  
221  
222  
223  
224  
225  
226  
227  
228  
229  
230  
231  
232  
233  
234  
235  
236

including image quality, the image-processing algorithm and properties of the particles and optics were analysed using techniques set out by Raffel et al. [19] and Wieneke [22]. These yielded estimates for the maximum errors for the velocity measurements of 4% for the wider field-of-view data and 3% for the remaining cases. This is slightly lower than errors estimated for the same PIV equipment by Avadiar et al. [4], largely due to the lower spanwise velocities induced by the geometry used for the present study, which resulted in reduced out-of-plane motion of the particles.

Boundary layer profiles were measured on both the endplates as well as the ground plane. At the nose of the model, the ground plane had a boundary layer thickness (defined here as the distance from the surface at which the streamwise velocity reaches  $0.99U_\infty$ ) of  $0.11H$  for the  $Re = 2 \times 10^4$  case, with a corresponding thickness of  $0.12H$  on the endplates.

### 3. Results and Discussion

#### 3.1. Time-averaged flow

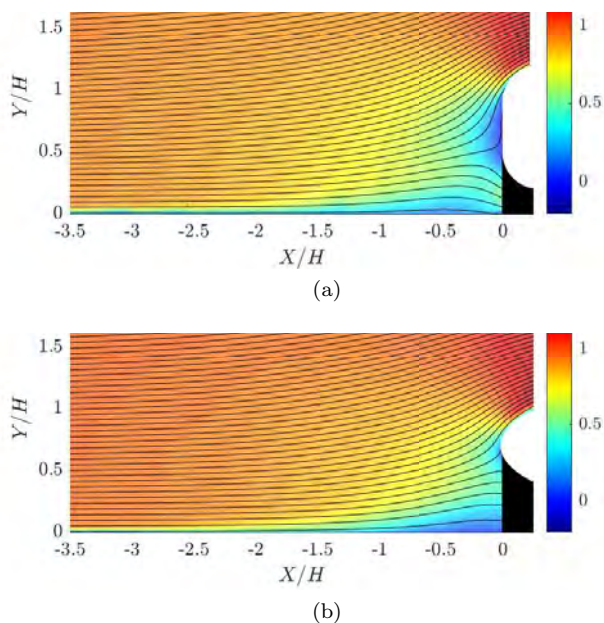


Figure 4: Contours of  $u/u_\infty$  upstream of the model nose for the (a) Ahmed body cross-section and (b) elliptical-nosed body with overlaid streamlines. Origin taken along ground plane at model nose position.

The stagnation point for the Ahmed body cross-section is located  $0.19H$  below the centreline as seen in Figure 4a. Likewise, the stagnation point of the elliptical-nosed body also appears to be positioned below the nose (Figure 4b). The associated high pressure region results in an adverse pressure gradient extending upstream of the nose, increasing growth in the boundary layer along the ground. Significant flow separation is present above the Ahmed-body cross-section, commencing at the end of the rounded portion of the nose, with a reattachment length,  $L_{OB}$ , of

approximately  $2.1H$  measured from the front of the body (refer to Figure 3 for clarity). While not observable in Figure 5, qualitative flow visualisation of the flow above the elliptical-nosed body indicated the presence of a thin region of recirculation, once again originating from the end of the curved nose section and extending approximately  $0.7H$  downstream. Due to the small thickness of the bubble relative to the body (reversed flow was observed up to a height of approximately  $0.01H$ ), the effect on the flow downstream was not expected to be significant in comparison to the region of separation above the Ahmed body cross-section, for which reversed flow was measured up to  $0.12H$  above the body.

The boundary layer at the trailing edge above the elliptical-nosed body has a boundary layer thickness of  $0.12H$ , a displacement thickness of  $0.06H$  and a momentum thickness of  $0.01H$ . The corresponding values for the Ahmed body cross-section were  $0.57H$ ,  $0.14H$  and  $0.05H$ . This increase is attributable to the extended separation region above the body, with the short distance between the reattachment point and fixed separation point at the rear of the body reducing the ability of the boundary layer to relax prior to the rear separation point. Some variation was also observed in the flow leaving the underbody, with the Ahmed body cross-section recording a peak of  $1.12U_\infty$  at a vertical position  $0.10H$  away from the ground, whilst the corresponding values for the elliptical-nosed body were  $1.15U_\infty$  and  $0.08H$ . This increase in velocity likely signifies a greater underbody flow volume for the elliptical-nosed body.

The thinner, higher momentum boundary layer above the elliptical-nosed body results in a near-symmetric wake as seen in Figure 6b, with the two recirculation regions of comparable size. This is in contrast to the Ahmed body (Figure 6a), where the greater turbulent mixing across the shear layer and the reduced momentum results in a greater initial separation angle for the upper shear layer and a wake dominated by the upper recirculation region. This behaviour of the highly turbulent upper shear layer aligns with the observations of Bearman [6], who commented that a chief consequence of upstream turbulence on sharp-edged bodies is increased growth in the separated shear layer and greater entrainment of fluid into the wake. However, despite the initial shear-layer growth, the recirculation length of the Ahmed body cross-section ( $2.1H$ ) is slightly higher than its elliptical-nosed counterpart ( $2.0H$ ), possibly due to greater interaction between the shear layers increasing the entrainment of fluid into the wake of the elliptical-nosed body.

The influence of the upstream separation is also evident in the Reynolds stress distribution of the Ahmed body wake. A region of high streamwise,  $\overline{u'u'}$ , fluctuations can be observed above the body in Figure 7a, extending well beyond the separation point. In addition to this, the  $\overline{u'u'}$  stress distribution for the Ahmed body cross-section is noticeably lower in magnitude relative to the corresponding distribution for the elliptical-nosed body (Figure 8a).

237  
238  
239  
240  
241  
242  
243  
244  
245  
246  
247  
248  
249  
250  
251  
252  
253  
254  
255  
256  
257  
258  
259  
260  
261  
262  
263  
264  
265  
266  
267  
268  
269  
270  
271  
272  
273  
274  
275  
276  
277  
278  
279  
280  
281  
282  
283  
284  
285  
286  
287  
288  
289  
290  
291  
292  
293  
294  
295

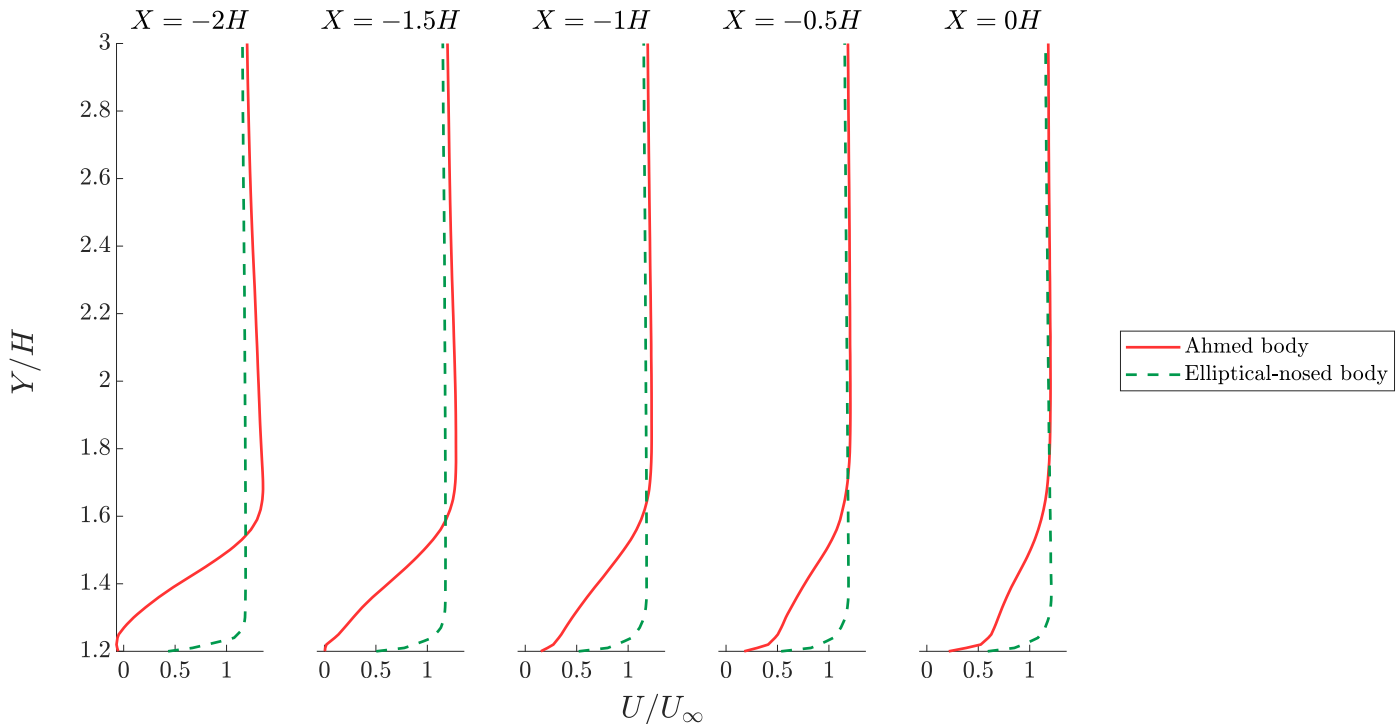


Figure 5: Velocity profiles above both bodies at various streamwise positions.

The cross-flow,  $\overline{v'v'}$ , stress distributions also differ significantly, with the elliptical-nosed body again seeing noticeably higher stresses in its wake. The peak stress location also occurs lower (in the  $Y$ -direction) than in the Ahmed body case. The Reynolds stresses for the Ahmed body cross-section are not dissimilar to the results of Parkin et al. [15], possessing similar magnitudes and overall distributions despite the lack of a moving ground plane. Conversely, the distributions for the elliptical-nosed body bears greater similarity to that of the Ahmed body cross-section in the absence of a ground plane, as presented by Parkin et al. [16], albeit with the peaks markedly further away from the body, likely signifying a longer dead-water region. In both instances, the cross-flow stresses peak close to the centreline of the body, with the present study seeing a peak of 0.13 in comparison to the away-from-ground case, which possesses a peak in excess of 0.2. The absence, in this instance, of the two small, opposite-signed zones away from the primary regions of high shear,  $\overline{u'v'}$ , stress (Figure 8c) is also noteworthy here. Additionally, it should be pointed out, that unlike the away-from-ground case, the two peaks for the streamwise stresses are substantially different, with the peak located closer to the upper shear layer possessing a magnitude almost 40% lower than the corresponding value of the peak in the lower half of the wake, whilst also being located further away from the body, suggesting a degree of asymmetry in the wake due to the presence of the ground plane.

Notably, in comparison to the Ahmed body cross-section, the symmetry present in the wake topology of the elliptical-nosed body appears to bear greater qualitative similarities

to the symmetry plane of the three-dimensional Ahmed body studied by Grandemange et al. [11], particularly in case of the in-plane velocity streamlines. While Grandemange et al. [11] conducted experiments at a higher Reynolds number ( $Re = 9 \times 10^4$ ), work done by Spohn and Gilliron [20] on related geometries showed that the flow topology remained relatively stable across Reynolds numbers in the range of  $O(10^3)$  to  $O(10^6)$ . Interestingly, this would suggest that at lower Reynolds numbers, the elliptical-nosed body tested here may present a better analogue to the time-averaged three-dimensional Ahmed body flow at higher Reynolds numbers than the Ahmed body cross-section. One should however keep in mind the additional complexities introduced by the two added (side) shear layers for the three-dimensional case. This is especially true of time-dependent comparisons given the significant increase in fluctuations of the spanwise velocity for that case along with the documentation of weak vortex-shedding activity in the lateral plane as well as that of observed bistability in the 3D wake [11].

### 3.2. Time-dependent flow

Proper Orthogonal Decomposition (POD) was used to analyse the centre-plane vorticity fields in the wake obtained from PIV measurements. This was undertaken across the centre-plane of the wake of the model, across a window spanning  $1.5H$  in the vertical direction and  $4.5H$  in the longitudinal direction. Although there are variants of POD analysis, the methodology for POD applied here was based on the work of Chatterjee [9], with additional information on its applicability to fluid flows sourced from

296  
 297  
 298  
 299  
 300  
 301  
 302  
 303  
 304  
 305  
 306  
 307  
 308  
 309  
 310  
 311  
 312  
 313  
 314  
 315  
 316  
 317  
 318  
 319  
 320  
 321  
 322  
 323  
 324  
 325  
 326  
 327  
 328  
 329  
 330  
 331  
 332  
 333  
 334  
 335  
 336  
 337  
 338  
 339  
 340  
 341  
 342  
 343  
 344  
 345  
 346  
 347  
 348  
 349  
 350  
 351  
 352  
 353  
 354

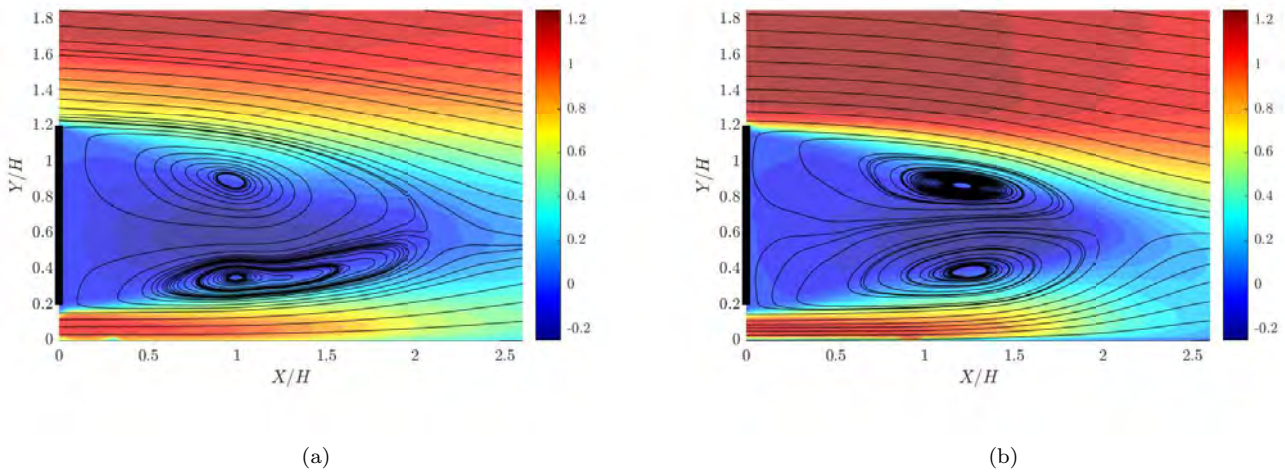


Figure 6: Velocity profiles overlaid on contours of  $U/U_\infty$  in the near-wake of (a) the Ahmed body cross-section and (b) the elliptical-nosed body.

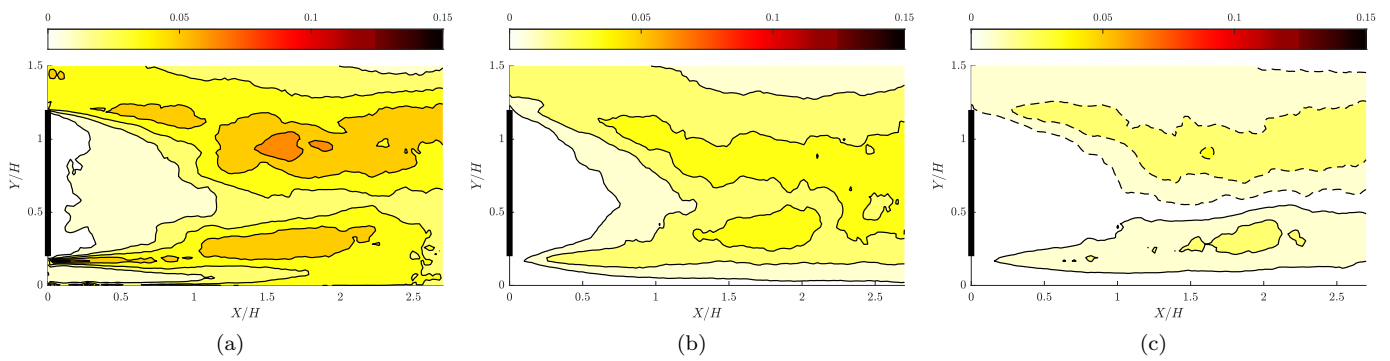


Figure 7: Contours of Reynolds stress magnitudes in the wake of the Ahmed body cross-section. (a)  $\overline{u'u'}/U_\infty^2$ , (b)  $\overline{v'v'}/U_\infty^2$  and (c)  $\overline{u'v'}/U_\infty^2$ . Dashed lines represent negative values.

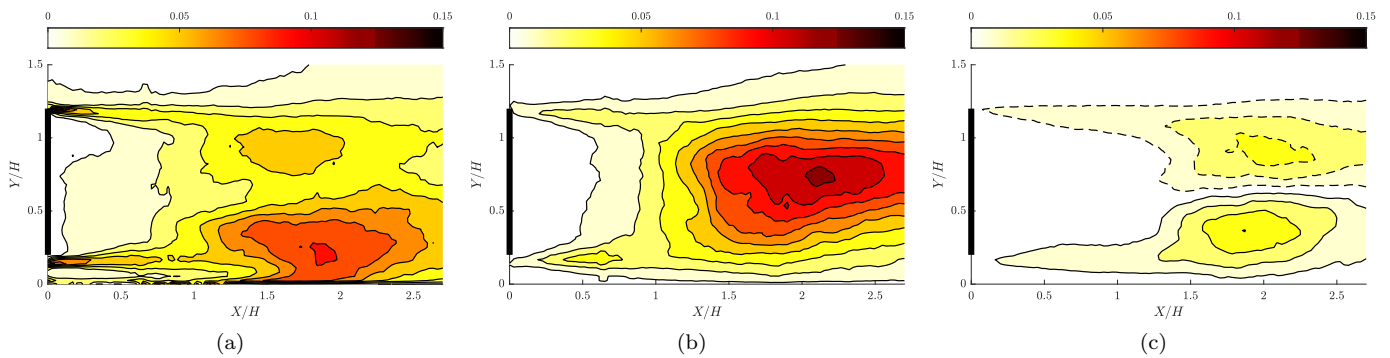


Figure 8: Contours of Reynolds stress magnitudes in the wake of the elliptical-nosed body. (a)  $\overline{u'u'}/U_\infty^2$ , (b)  $\overline{v'v'}/U_\infty^2$  and (c)  $\overline{u'v'}/U_\infty^2$ . Dashed lines represent negative values.

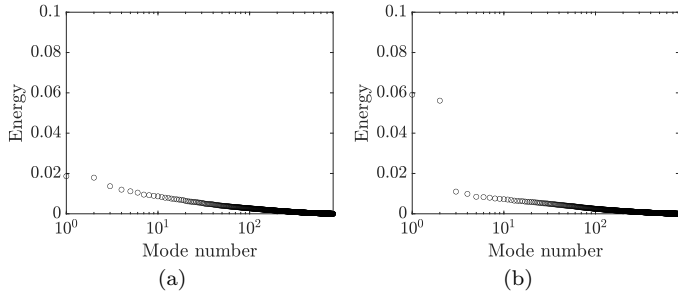


Figure 9: Relative POD modal energy for (a) Ahmed body cross-section and (b) elliptical-nosed body.

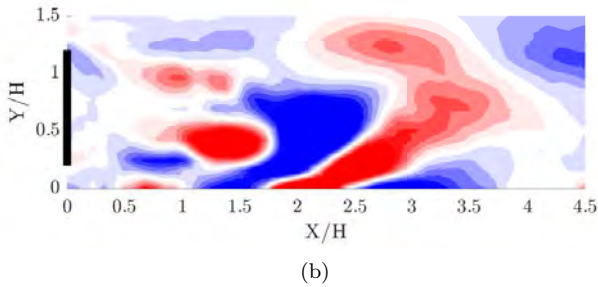
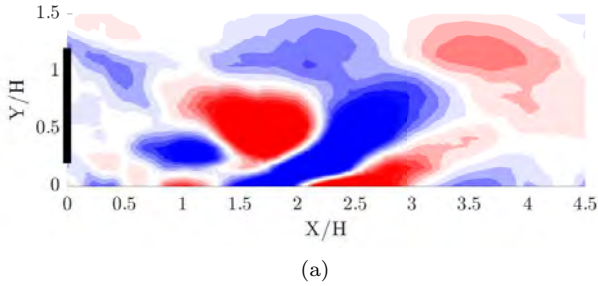


Figure 10: First two vorticity modes for the Ahmed body cross-section. The contours visualize the relative strength, with red signifying values above a positive threshold and blue, below a negative threshold.

Berkooz et al. [7].

The POD results for Ahmed-body cross-section wake yield relatively low energy modes, with limited decay in the modal energy contribution as the mode number increases (Figure 9a). Such a distribution is indicative of flow dynamics largely dominated by unstructured turbulence, which agrees well with existing literature on the Ahmed body cross-section [15].

Nevertheless, some underlying coherent activity is observable for both geometries. The first two modes for each case form a pair with a noticeably higher energy contribution (Figure 9) relative to the rest. For the Ahmed body cross-section, these modes contain 4% of the total energy, while for the elliptical-nosed body, the corresponding value is 11%. The spatial structure of these modes appear to share some similarities near the lower shear layer, but diverge significantly when approaching the upper shear

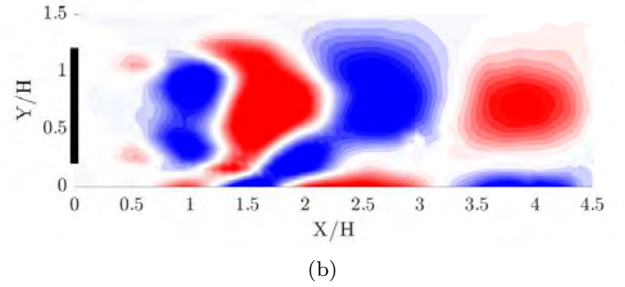
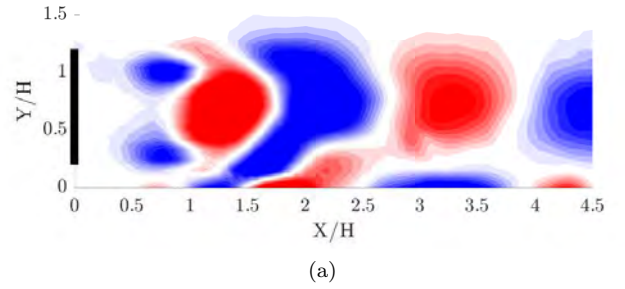


Figure 11: First two vorticity modes for the elliptical-nosed body wake. The contours visualize the relative strength, with red signifying values above a positive threshold and blue, below a negative threshold.

layer. This is unsurprising given the differing flow conditions above each model. The modes for the Ahmed body cross-section (Figure 10) also appear to contain a good deal more “noise” than its elliptical-nosed counterpart, as seen in Figure 11. The presence of these prominent mode pairs allows for the use of phase-averaging using those modes. This approach uses the most energetic mode pair from POD as the basis for calculating the phase angle,  $\phi$ , instead of the time history of a single point.

The phase-averaged results for the elliptical-nosed body presented in Figure 13 depicts a predominantly one-sided shedding process, with the counter-clockwise rotating vortex (colored red in Figure 13) formation likely inhibited by the presence of the ground plane, resulting in low-intensity, rapidly decaying vortices. The Ahmed body cross-section (Figure 12) sees even less pronounced vortex shedding from both positions. Spectral analysis, utilising a fast Fourier transform algorithm of the temporal contents of the POD modes depicted in Figure 15 reveals near identical frequency content between the first two modes, with a prominent peak at a Strouhal number,  $St$ , of 0.25 for the elliptical-nosed body ( $St$  was based on the height of the model and freestream velocity for both cases). The Ahmed-body cross-section however, sees a cluster of smaller peaks in the range of  $St = 0.1$  to 0.3, with the highest peak now occurring at  $St = 0.22$  as seen in Figure 14. This lack of a clear dominant frequency further points towards the lack of regular periodic activity in the wake.

While the frequencies associated with these modes are somewhat higher than those recorded by Grandemange

414  
415  
416  
417  
418  
419  
420  
421  
422  
423  
424  
425  
426  
427  
428  
429  
430  
431  
432  
433  
434  
435  
436  
437  
438  
439  
440  
441  
442  
443  
444  
445  
446  
447  
448  
449  
450  
451  
452  
453  
454  
455  
456  
457  
458  
459  
460  
461  
462  
463  
464  
465  
466  
467  
468  
469  
470  
471  
472

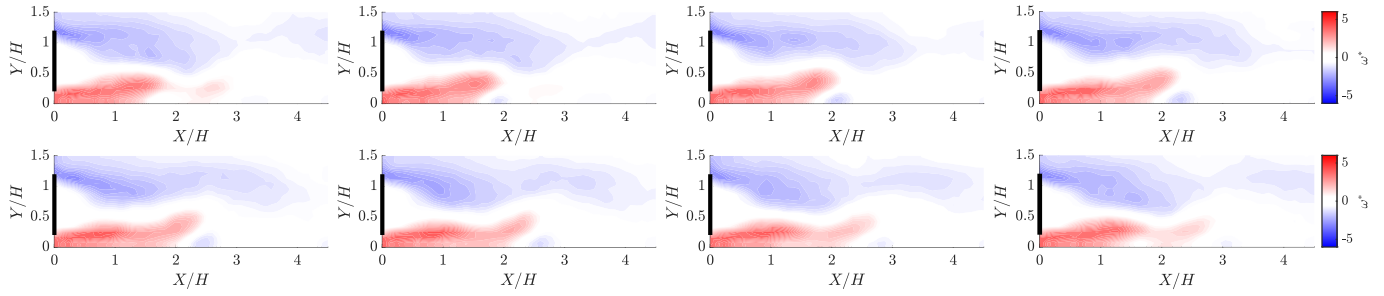


Figure 12: Full cycle of phase-averaged vorticity contours in the wake of the Ahmed-body cross-section at  $Re = 2 \times 10^4$ , where  $\omega^*$  is defined as the vorticity normalised based on the body height and freestream velocity.

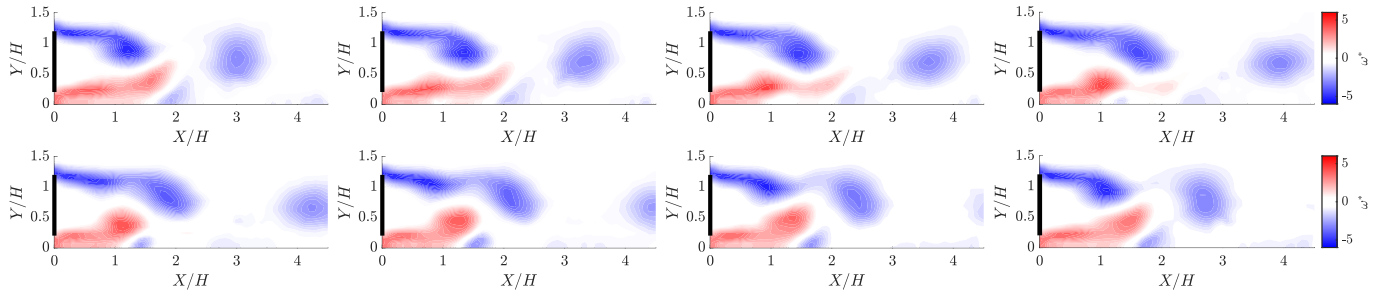


Figure 13: Full cycle of phase-averaged vorticity contours in the wake of the elliptical-nosed body at  $Re = 2 \times 10^4$ , where  $\omega^*$  is defined as the vorticity normalised based on the body height and freestream velocity.

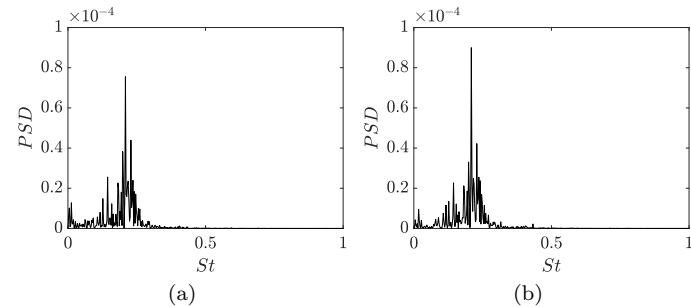


Figure 14: Power spectral density of temporal content of the first two POD modes for the Ahmed body cross-section, (a) Mode 1 and (b) Mode 2.

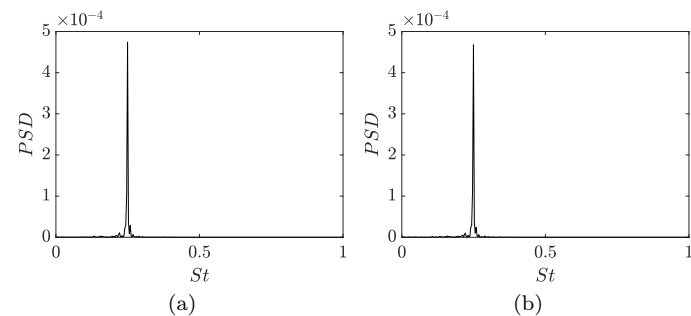


Figure 15: Power spectral density of temporal content of the first two POD modes for the elliptical-nosed body, (a) Mode 1 and (b) Mode 2.

et al. [11] for the three-dimensional Ahmed body, the low energy contribution of these modes is otherwise consistent with existing literature. In the context of extrapolating results from the two-dimensional data presented here to three-dimensional subjects, some caution is warranted given that the shedding described by Grandemange et al. [11] appears to be two-sided, in contrast to the primarily one-sided shedding observed for the elliptical-nosed body.

It is of interest to note that the shedding motion of the elliptical-nosed body is clearly identifiable in the instantaneous velocity vectors presented in Figure 16. The presence of the counter-clockwise vortex is clearly visible here, despite the relative weakness of the vortex, as implied by Figure 13.

### 3.3. Reynolds number sensitivities

Thus far, all results presented have been taken from tests conducted at  $Re = 2 \times 10^4$ . In addition to these, tests were also conducted at  $Re = 5 \times 10^3$  and  $1 \times 10^4$ , which were suggestive of a degree of Reynolds number sensitivity in both models. This is apparent even before the flow reaches the body, with the ground plane boundary layer experiencing rapid growth due to the deceleration of the flow, caused by the adverse pressure gradient upstream of the body.

As seen in Figures 17 and 18, this results in flow separation for the two lower Reynolds number cases, with the extent of separation increasing with the reduction in Reynolds number. This flow separation and the associated growth in the displacement thickness increases the angle of incidence of the flow at the leading edge, and in the case

473  
474  
475  
476  
477  
478  
479  
480  
481  
482  
483  
484  
485  
486  
487  
488  
489  
490  
491  
492  
493  
494  
495  
496  
497  
498  
499  
500  
501  
502  
503  
504  
505  
506  
507  
508  
509  
510  
511  
512  
513  
514  
515  
516  
517  
518  
519  
520  
521  
522  
523  
524  
525  
526  
527  
528  
529  
530  
531

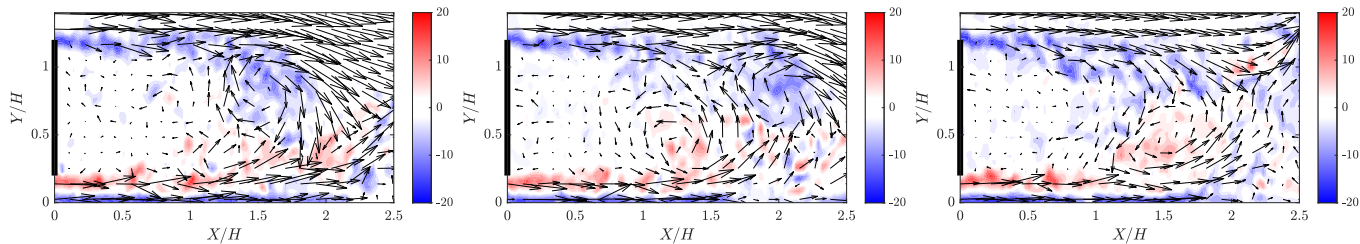
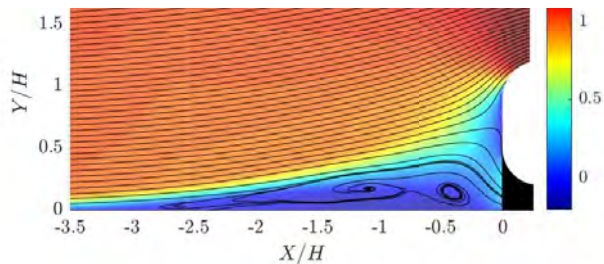
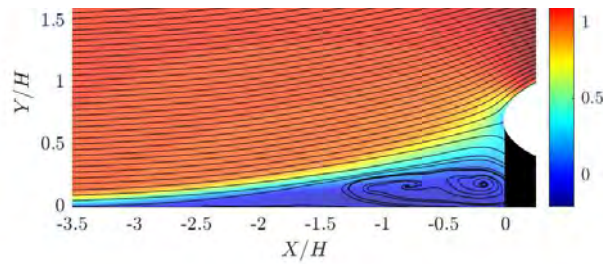


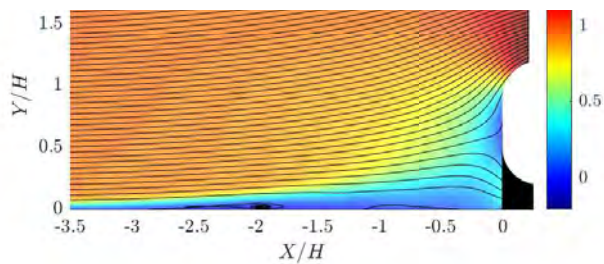
Figure 16: Instantaneous velocity vectors in the wake of the elliptical-nosed body superimposed on contours of instantaneous vorticity highlighting different stages of the vortex shedding process over a single cycle. Snapshots taken at intervals of  $0.25 \times$  shedding period. Only every fourth vector is plotted for clarity.



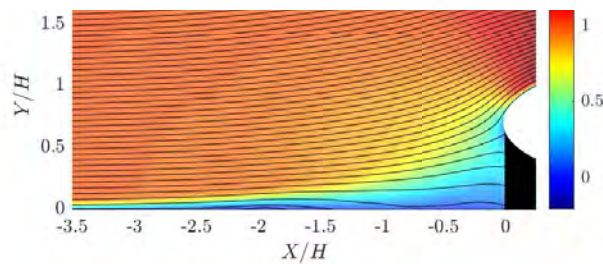
(a)



(a)



(b)



(b)

Figure 17: Contours of  $U/U_\infty$  upstream of the model nose for the Ahmed body cross-section with overlaid streamlines for (a)  $Re = 5 \times 10^3$  and (b)  $Re = 1 \times 10^4$ . Origin taken along ground plane at model nose position.

Figure 18: Contours of  $U/U_\infty$  upstream of the model nose for the elliptical-nosed body with overlaid streamlines for (a)  $Re = 5 \times 10^3$  and (b)  $Re = 1 \times 10^4$ . Origin taken along ground plane at model nose position.

of the Ahmed body cross-section, raises the position of the stagnation point.

The above-body flow velocities depicted in Figure 19, demonstrate that the Ahmed body cross-section also sees a marked decrease in the extent of the recirculation bubble above the body for the two lower Reynolds numbers. This appears to be linked to the previously mentioned change in the upstream boundary layer, with the increase in flow angle and the accompanying acceleration in the flow over the nose radius corresponding to a weaker adverse pressure gradient over the nose and subsequently, a reduction to the size of the recirculation region. Unsurprisingly, this variation has a significant effect on the upper shear layer, with Figure 20 now indicative of higher velocities above the body close to the rear separation point, due to the reduced disruption to the flow caused by the above-body separation region. A similar effect is likely to have occurred with the elliptical-nosed body, where the previously mentioned thin region of separation above the body was not observed at

the two lower Reynolds numbers.

The velocity profiles also show the influence of the ground-plane boundary-layer separation with a distinct velocity deficit occurring in the flow leaving the underbody as the Reynolds number decreases (Figure 20). This feature can be attributed to the ground-plane boundary-layer separation upstream of the body and is also noticeable for the elliptical-nosed body (Figure 21).

These profiles behind the elliptical-nosed body appear to diverge slightly further downstream, with the highest Reynolds number case seemingly producing a slightly shorter recirculation region. This could be ascribed to greater mixing across the shear layer encouraged by the reduced viscous effects seen by higher Reynolds number flows. This drop in the wake length is also observable for the Ahmed body cross-section at the highest Reynolds number (Figure 20).

The dynamics of the low Reynolds number cases also provide some additional points of interest. Results from

532  
533  
534  
535  
536  
537  
538  
539  
540  
541  
542  
543  
544  
545  
546  
547  
548  
549  
550  
551  
552  
553  
554  
555  
556  
557  
558  
559  
560  
561  
562  
563  
564  
565  
566  
567  
568  
569  
570  
571  
572  
573  
574  
575  
576  
577  
578  
579  
580  
581  
582  
583  
584  
585  
586  
587  
588  
589  
590

Table 1: Flow quantities for different Reynolds numbers for the Ahmed body cross-section.

$Re$	$St$	$E_{12}$	$L_{OB}$	Recirculation length
$5 \times 10^3$	-	0.03	$1.0H$	$2.1H$
$1 \times 10^4$	0.20	0.03	$1.2H$	$2.3H$
$2 \times 10^4$	0.22	0.04	$2.1H$	$2.1H$

Table 2: Flow quantities for different Reynolds numbers for the elliptical-nosed body.

$Re$	$St$	$E_{12}$	Recirculation length
$5 \times 10^3$	-	0.03	$2.2H$
$1 \times 10^4$	0.24	0.07	$2.3H$
$2 \times 10^4$	0.25	0.11	$2.0H$

POD (Tables 1 and 2) conducted on each case reveal that the energy contribution of the first two modes, (referred to henceforth as  $E_{12}$ ), declines noticeably for both cases, with the results for the two lowest Reynolds number cases for the elliptical-nosed body in particular suggesting significantly reduced coherent activity in the wake. This is further supported by the fact that for the lowest Reynolds number case, the first two modes no longer represent a mode pair, instead representing substantially lower frequency modes. The reasons for this require further examination, but may well be linked to the changing characteristics of the underbody flow.

For the two higher Reynolds number cases, the frequency associated with the first two modes appears to be slightly lower for the Ahmed body cross-section. This may partially be due to the exaggerated boundary layer at the top trailing edge, due to the upstream separation, increasing the “effective height” of the model at the trailing edge. This does not however, account for the slight reduction in Strouhal number when the Reynolds number is reduced to  $1 \times 10^4$  for both cases, especially given the reduction in leading-edge separation for the Ahmed body cross-section. This aspect could be driven by the loss in momentum for the lower shear layer driven by the upstream separation at this Reynolds number.

A comparison here to the findings of Adams and Johnston [2], is apt, given the variation in Reynolds number and above-body boundary-layer profiles (that study looked at the effects of Reynolds number and boundary layer thickness on separation behind a backward-facing step). In the case of the Ahmed body cross-section, the upper boundary layer is quite similar across the two lower Reynolds numbers, allowing the effects of the varying Reynolds number on the wake to come to the fore. Adams and Johnston observed an increase in reattachment length with Reynolds up to about  $Re = 2 \times 10^4$ , which thus far, appears to align with the results in Table 1, if the recirculation lengths in this study were to behave in a similar manner. However, the highest Reynolds number case instead sees a marked

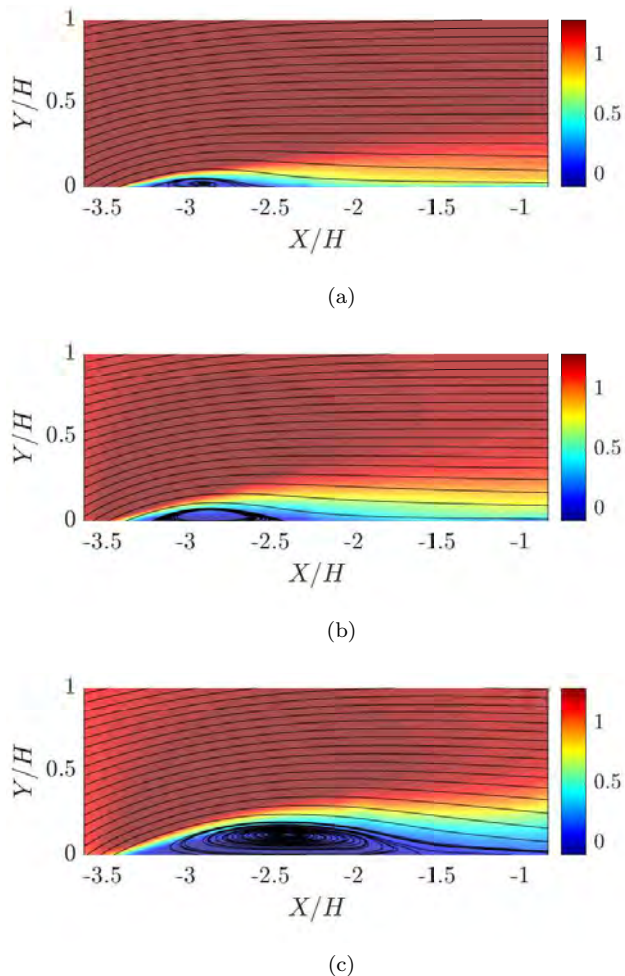


Figure 19: Velocity streamlines superimposed on contours of  $U/U_\infty$  above the Ahmed body for (a)  $Re = 5 \times 10^3$ , (b)  $Re = 1 \times 10^4$  and (c)  $Re = 2 \times 10^4$ .

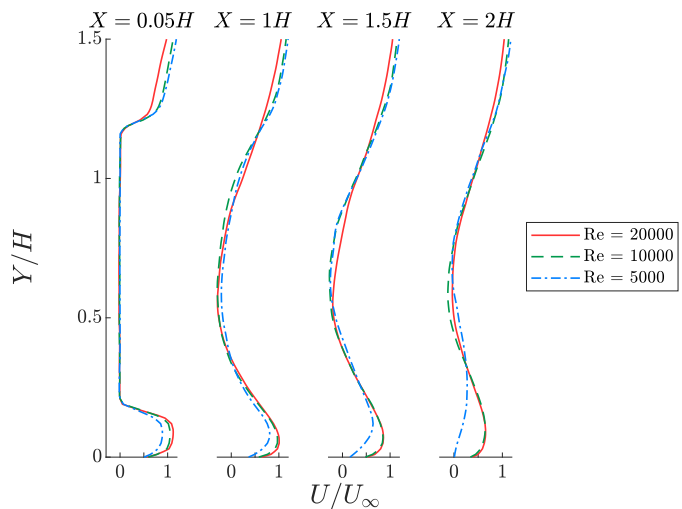


Figure 20: Velocity profiles taken at different streamwise positions downstream of the Ahmed body cross-section.

591  
592  
593  
594  
595  
596  
597  
598  
599  
600  
601  
602  
603  
604  
605  
606  
607  
608  
609  
610  
611  
612  
613  
614  
615  
616  
617  
618  
619  
620  
621  
622  
623  
624  
625  
626  
627  
628  
629  
630  
631  
632  
633  
634  
635  
636  
637  
638  
639  
640  
641  
642  
643  
644  
645  
646  
647  
648  
649

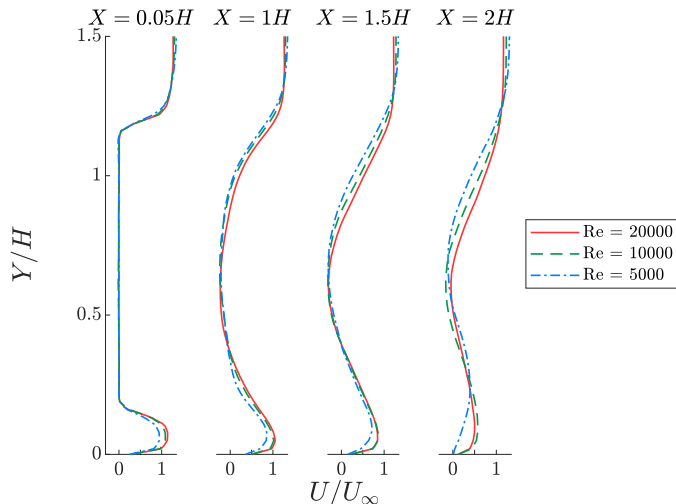


Figure 21: Velocity profiles taken at different streamwise positions downstream of the elliptical-nosed body.

decrease in recirculation length. Note that this case possesses a significantly thicker boundary layer prior to separation, and Adams and Johnston [2] did record a weak trend of the reattachment length declining with increasing boundary-layer thickness. The reduction in the recirculation length of the elliptical-nosed body wake however, is not well explained by this mechanism, given the absence of any notable increase to the boundary-layer thickness with increasing Reynolds number. An explanation for this could instead be linked to the greater role played by coherent vortex shedding, as evidenced by the increase in modal energy of the first two POD modes. This points to a greater degree of shear-layer interaction across the wake, in turn leading to more flow entrainment into the recirculation region and a reduction in its length.

### 3.4. Effects of ground clearance

In addition to the effects of altering the Reynolds number, a brief study was also undertaken into the effects of varying the ground clearance of each model. While only four clearances were assessed, as Tables 3 and 4 demonstrate, a number of trends were readily apparent.

Firstly, a significant decrease in the wake recirculation length occurred as the ground clearance increased for both nose geometries. Note that the increase in this measure for the zero ground clearance cases was great enough to extend it beyond the limits of the PIV window used, preventing an accurate estimate for these cases. This was to be expected however, as for a Reynolds number of  $2 \times 10^4$ , Adams and Johnston [1] found the reattachment length to exceed  $6H$  regardless of boundary layer thickness.

Another observable trend is the increase in leading-edge separation for the Ahmed body cross-section as the ground clearance is decreased, which follows a remarkably similar trend to the wake length, with one exception; the zero-ground clearance case, which now features minimal leading-edge separation (Table 3). It should be noted here,

that during visual observations of this case, significant flow separation on the ground upstream of the model was observed, and as seen in Table 1, this does appear to inhibit flow separation over the nose. The continued presence of significant leading-edge separation over the upper surface of the model, even when the ground clearance is doubled, offers further insight into the effects of this flow characteristic on the wake. As Figure 22 shows, the asymmetry in the wake persists, albeit somewhat less exaggerated. While some caution should be taken when linking this solely to the asymmetry of the leading-edge separation, given the change to the underbody flow caused by altering the ground clearance, the results from both the  $0.2H$  and  $0.4H$  ground clearance cases are suggestive of a strong connection between the characteristics of the boundary layers approaching the trailing edge. Given that the symmetry of the elliptical-nosed-body wake remains with the increasing ground clearance (Figure 23), the asymmetry in the wake of the Ahmed body cross-section does appear to be linked to the prominent leading-edge separation on the top surface of the body, and its effects on the boundary layer downstream.

Finally, and perhaps unsurprisingly, there also appears to be a substantial increase in the coherence of vortex shedding in the wake as ground clearance is increased. This can be seen in the increasing proportion of the energy content of the first two POD modes (Tables 3 and 4). Curiously, for the away-from-ground case, the first two modes for the Ahmed-body cross-section account for noticeably more energy relative to their elliptical-nosed counterparts. Given the continued weakening of the leading-edge separation for the Ahmed body cross-section as the ground clearance grows, one might expect the modal energies for the elliptical-nosed body to more rapidly reach parity with the away-from-ground case. However, it is curious that these modes contain a lower share of energy relative to the Ahmed body cross-section. A possible explanation could be that the Ahmed body wake possesses weaker fluctuations overall, leading to a higher proportion of energy for a similar absolute amount, but further investigation is required to determine this. For the zero-ground clearance cases, in addition to the lowered energy content, the first two modes also fail to form a mode pair, signifying negligible Karman vortex shedding, which is to be expected given the absence of the second shear layer which drives this process of alternate shedding. For the remaining cases, the Strouhal number of these modes do not follow an obvious trend, seeing a sharp increase from  $0.2H$  to  $0.4H$  before remaining stable for the elliptical-nosed body and decreasing slightly for the Ahmed body cross-section.

The trends concerning the effects of the ground clearance agree well with existing literature on the away-from-ground, two-dimensional Ahmed body. For instance, Pastoor et al. [17] note the significant effect of von Karman vortex shedding on the wake for this case, which is evidenced here by the trend of the increasing energy proportion ascribed to the first POD mode pair. The Strouhal

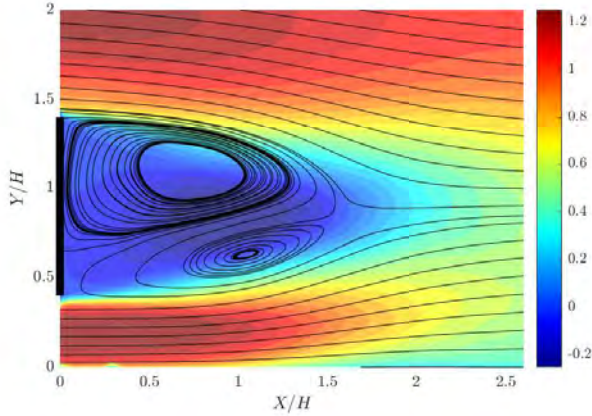


Figure 22: Velocity profiles overlaid on contours of  $U/U_\infty$  in the near-wake of the Ahmed body cross-section for a ground clearance of  $0.4H$ .

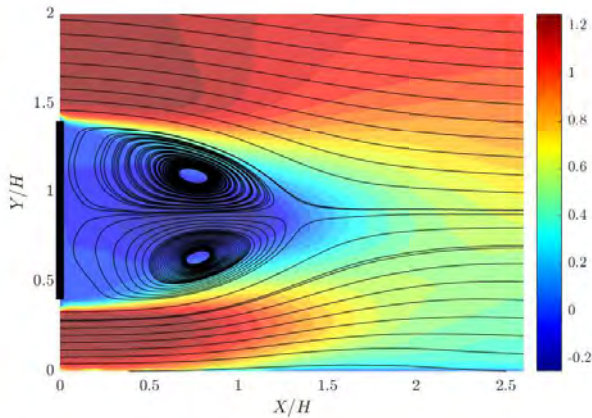


Figure 23: Velocity profiles overlaid on contours of  $U/U_\infty$  in the near-wake of the elliptical nosed body for a ground clearance of  $0.4H$ .

number presented here, for the Ahmed body cross-section, (0.24) also agrees well with those results (0.23). Furthermore, the significantly shorter wake without the ground plane had also been documented by Parkin et al. [16].

#### 4. Conclusions

A comparison has been presented of two square-backed bodies with differing overbody flow properties induced by different nose shapes. In contrast to the relative insensitivity to nose-shape in the absence of a ground plane borne out in the studies conducted by Bearman [5], Park et al. [14] and Pastoor et al. [17], the results here demonstrate the substantially increased importance of nose-shape on the wake structure of these bodies in proximity to the ground. Both the mean and dynamic wake structure see significant changes, with the time-averaged results suggesting that the disruption caused to the upper-surface boundary layer by the sizeable recirculation region exaggerates the asymmetry of the wake, with the upper shear layer experiencing significant thickening due to the additional advected turbulence. Analysis of the time-dependent

Table 3: Flow quantities for different ground clearances for the Ahmed body cross-section.

Ground clearance	$St$	$E_{12}$	Recirculation length	$L_{OB}$
$0H$	-	0.04	$> 4.8H$	$0.5H$
$0.2H$	0.22	0.04	$2.1H$	$2.1H$
$0.4H$	0.26	0.18	$1.6H$	$1.6H$
$4.2H$	0.24	0.27	$0.8H$	$0.9H$

Table 4: Flow quantities for different ground clearances for the elliptical-nosed body.

Ground clearance	$St$	$E_{12}$	Recirculation length
$0H$	-	0.05	$> 4.8H$
$0.2H$	0.25	0.11	$2.0H$
$0.4H$	0.28	0.18	$1.3H$
$4.2H$	0.28	0.18	$0.9H$

flow does show evidence of underlying coherent vortex shedding for the elliptical-nosed body, with the coherence of shedding reduced for the Ahmed body. Given these results, it may prove beneficial to consider the use of more streamlined nose shapes for higher Reynolds number wake studies in general.

Measurements have also been undertaken on the effect of the Reynolds number on the flow around these bodies. The results demonstrate the considerable sensitivity to Reynolds number of the upstream, above-body and wake flows for these bodies, which again contrast with the limited Reynolds number sensitivity observed in the absence of a ground plane [17]. This is especially important, as water channel studies are usually Reynolds number limited, but have been used to provide semi-qualitative guidance for higher Reynolds number behaviour. In this instance, the lower Reynolds number cases see prominent flow separation along the ground plane upstream of the body. This appears to restrict the flow entering the underbody region, which in turn affects the wake characteristics of the lower Reynolds number cases. Perhaps this, underlines the importance of utilising moving ground planes for future experiments in order to better quantify changes to the flow as the Reynolds number is varied. In addition to the Reynolds number, the effect of the ground plane has also been briefly considered. In short, the primary noticeable effects of increasing the distance to the ground plane appear to be an increase in the prominence of vortex shedding, linked to a significantly shorter wake separation region. In addition to this, the leading-edge separation on the top surface of the Ahmed body weakens appreciably as the ground clearance increases for cases where flow separation does not occur upstream of the model.

Overall, one might expect that a body with fixed rear separation points (such as a cylindrical square-backed Ahmed body) would result in a wake that would be relatively

Reynolds number insensitive. This means that low Reynolds number experiments could act as a semi-quantitative guide to higher Reynolds number behaviour. However, this work suggests that caution should be exercised when considering this approach, especially in instances of bodies in proximity to the ground at low Reynolds numbers. Additionally, this study further emphasises the importance of nose shape on wake structure, especially subject to ground proximity.

## References

- [1] E.W. Adams and J.P. Johnston. Effects of the separating shear layer on the reattachment flow structure part 1: Pressure and turbulence quantities. *Experiments in Fluids*, 6:400–408, 1988.
- [2] E.W. Adams and J.P. Johnston. Effects of the separating shear layer on the reattachment flow structure part 2: Reattachment length and wall shear stress. *Experiments in Fluids*, 6:493–499, 1988.
- [3] S.R. Ahmed, G. Ramm, and G. Faltin. Some salient features of the time-averaged ground vehicle wake. *SAE Technical Paper Series*, 840300, 1984.
- [4] T. Avadiar, M.C. Thompson, J. Sheridan, and D. Burton. The influence of reduced Reynolds number on the wake of the DriveAer estate vehicle. *Journal of Wind Engineering and Industrial Aerodynamics*, 188:207–216, 2019.
- [5] P.W. Bearman. The effect of base bleed on the flow behind a two-dimensional model with a blunt trailing edge. *The Aeronautical Quarterly*, 18:17, 1967.
- [6] P.W. Bearman. Review - Bluff body flows applicable to vehicle aerodynamics. *Journal of Fluids Engineering*, 102:9, 1980.
- [7] G. Berkooz, P. Holmes, and J.L. Lumley. The proper orthogonal decomposition in the analysis of turbulent flows. *Annual Review of Fluid Mechanics*, 25:539–575, 1993.
- [8] G. Bonnavion. *Dynamics of the unstable wake modes in automotive aerodynamics : from simplified models to real vehicles*. Thesis, 2018.
- [9] A. Chatterjee. An introduction to the proper orthogonal decomposition. *Current Science*, 78(7):808–817, 2000.
- [10] A. Fouras, D. Lo Jacono, and K. Hourigan. Target-free stereo piv: a novel technique with inherent error estimation and improved accuracy. *Experiments in Fluids*, 44(2):317–329, 2007.
- [11] M. Grandemange, M. Gohlke, and O. Cadot. Turbulent wake past a three-dimensional blunt body. part 1. global modes and bi-stability. *Journal of Fluid Mechanics*, 722:51–84, 2013.
- [12] S. Krajinović and J. Fernandes. Numerical simulation of the flow around a simplified vehicle model with active flow control. *International Journal of Heat and Fluid Flow*, 32(1):192–200, 2011.
- [13] G. Minelli, E.A. Hartono, V. Chernoray, L. Hjelm, and S. Krajinović. Aerodynamic flow control for a generic truck cabin using synthetic jets. *Journal of Wind Engineering and Industrial Aerodynamics*, 168:81–90, 2017.
- [14] H. Park, D. Lee, W.-P. Jeon, S. Hahn, J. Kim, J. Kim, J.I.N. Choi, and H. Choi. Drag reduction in flow over a two-dimensional bluff body with a blunt trailing edge using a new passive device. *Journal of Fluid Mechanics*, 563, 2006.
- [15] D. Parkin, J. Sheridan, and M.C. Thompson. Numerical analysis of periodic open-loop flow control on bluff bodies in ground proximity. *Journal of Wind Engineering and Industrial Aerodynamics*, 145:339–350, 2015.
- [16] D.J. Parkin, M.C. Thompson, and J. Sheridan. Numerical analysis of bluff body wakes under periodic open-loop control. *Journal of Fluid Mechanics*, 739:94–123, 2013.
- [17] M. Pastoor, L. Henning, B.R. Noack, R. King, and G. Tadmor. Feedback shear layer control for bluff body drag reduction. *Journal of Fluid Mechanics*, 608, 2008.
- [18] S.J. Price, D. Sumner, J.G. Smith, K. Leong, and M.P. Paidoussis. Flow visualization around a circular cylinder near to a plane wall. *Journal of Fluids and Structures*, 16(2):175–191, 2002.
- [19] M. Raffel, C. Willert, S. Werely, and J. Kompenhans. Particle image velocimetry, 2008.
- [20] A. Spohn and P. Gilliron. Flow separations generated by a simplified geometry of an automotive vehicle, 2002.
- [21] Z.J. Taylor, E. Palombi, R. Gurka, and G.A. Kopp. Features of the turbulent flow around symmetric elongated bluff bodies. *Journal of Fluids and Structures*, 27(2):250–265, 2011.
- [22] B. Wieneke. Piv uncertainty quantification from correlation statistics. *Measurement Science and Technology*, 26(7), 2015.